Lunar Prospector observations of the electrostatic potential of the lunar surface and its response to incident currents

J. S. Halekas,[1] G. T. Delory,[1] R. P. Lin,[1,2] T. J. Stubbs,[3,4] and W. M. Farrell[4]

Received 3 March 2008; revised 5 May 2008; accepted 3 June 2008; published 4 September 2008.

[1] We present an analysis of Lunar Prospector Electron Reflectometer data from selected time periods using newly developed methods to correct for spacecraft potential and self-consistently utilizing the entire measured electron distribution to remotely sense the lunar surface electrostatic potential with respect to the ambient plasma. These new techniques enable the first quantitative measurements of lunar surface potentials from orbit. Knowledge of the spacecraft potential also allows accurate characterization of the downward-going electron fluxes that contribute to lunar surface charging, allowing us to determine how the lunar surface potential reacts to changing ambient plasma conditions. On the lunar night side, in shadow, we observe lunar surface potentials of ~-100 V in the terrestrial magnetotail lobes and potentials of ~-200 V to ~-1 kV in the plasma sheet. In the lunar wake, we find potentials of ~-200 V near the edges but smaller potentials in the central wake, where electron temperatures increase and secondary emission may reduce the magnitude of the negative surface potential. During solar energetic particle events, we see nightside lunar surface potentials as large as ~-4 kV. On the other hand, on the lunar day side, in sunlight, we generally find potentials smaller than our measurement threshold of $\sim$20 V, except in the plasma sheet, where we still observe negative potentials of several hundred volts at times, even in sunlight. The presence of significant negative charging in sunlight at these times, given the measured incident electron currents, implies either photocurrents from lunar regolith in situ two orders of magnitude lower than those measured in the laboratory or nonmonotonic near-surface potential variation with altitude. The functional dependence of the lunar surface potential on electron temperature in shadow implies somewhat smaller secondary emission yields from lunar regolith in situ than previously measured in the laboratory. These new techniques open the door for future studies of the variation of lunar surface charging as a function of temporal and spatial variations in input currents and as a function of location and material characteristics of the surface as well as comparisons to the increasingly sophisticated theoretical predictions now available.

Citation: Halekas, J. S., G. T. Delory, R. P. Lin, T. J. Stubbs, and W. M. Farrell (2008), Lunar Prospector observations of the electrostatic potential of the lunar surface and its response to incident currents, *J. Geophys. Res.*, *113*, A09102, doi:10.1029/2008JA013194.

1. Introduction

[2] The surface of the Moon, lacking a global magnetic field or a significant atmosphere to shield it from external influences, lies exposed to solar photons and solar and magnetospheric plasma. The lunar surface, therefore, forms an ideal natural laboratory to study the interaction of charged particles and photons with surfaces. The same fundamental processes also operate at other airless bodies such as Mercury, asteroids, and some outer planet moons. To a great degree, the same processes also affect spacecraft.

[3] An exposed surface such as that of the Moon charges in response to incident currents. Photoelectrons generated from the surface by solar photons constitute an escaping negative current or equivalently an incident positive current. Plasma electrons and ions produce negative and positive incident currents, respectively. Secondary electrons produced by electron and ion impact constitute an escaping negative current or equivalently an incident positive current. The magnitude of current from each source depends on the electrostatic potential of the surface with respect to the

[1]Space Sciences Laboratory, University of California, Berkeley, California, USA.
[2]Physics Department, University of California, Berkeley, California, USA.
[3]Goddard Earth Sciences and Technology Center, University of Maryland Baltimore County, Baltimore, Maryland, USA.
[4]NASA Goddard Spaceflight Center, Greenbelt, Maryland, USA.

Copyright 2008 by the American Geophysical Union.
0148-0227/08/2008JA013194

Table 1. Typical Ambient Plasma Properties and Resulting Lunar Surface Potentials

	Tail Lobe	Plasma Sheet	Solar Wind	Wake	SEP Event
Electron density	0.001–0.5 cm^{-3}	0.01–1 cm^{-3}	0.5–10 cm^{-3}	0.001–0.1 cm^{-3}	0.001–0.1 cm^{-3} in wake
Electron temperature	<100 eV	100 eV to 2 keV	5–30 eV	50–150 eV	50 eV to 1 keV in wake
Lunar surface potential	−150 to 0 V	−1000 to 0 V	<20 V	−200 to 0 V	−1000 to −4000 V in wake

surrounding plasma. In equilibrium, the surface charges to a floating potential at which the sum of the incident positive and negative currents balances. Mathematically speaking, $\sum_k J_k(U) = 0$, where J_k are the various currents J_ν (photoelectron current), J_I (ion current), J_E (electron current), J_{SEC} (secondary electron current), etc. Each term in this equation depends on the surface potential U, and in general this forms a transcendental equation that we can solve for the value of that potential (if we know the functional forms and magnitudes of all incident currents).

[4] The Moon is exposed to currents which vary over many orders of magnitude during its orbit around the Earth. In the solar wind, the day side of the Moon is exposed to relatively low temperature flowing plasma (supersonic for ions), while the night side lies in the lunar plasma wake, exposed to much more rarefied plasma at a somewhat higher temperature [*Halekas et al.*, 2005b]. In the terrestrial magnetosphere, on the other hand, the Moon is exposed to both very rarefied plasma in the magnetotail lobes and more energetic and turbulent plasma in the plasma sheet and magnetosheath. Meanwhile, solar illumination (and therefore photocurrent) varies as a function of solar zenith angle (SZA) on the day side but is absent on the night side. Finally, transient solar events such as solar energetic particle (SEP) events can contribute very energetic plasma currents to the surface for brief periods. Given this extreme variability, the lunar surface should charge to potentials that vary over orders of magnitude, and we will see that observations do indeed support these expectations. We summarize the electron properties measured by Lunar Prospector in these various environments in Table 1, along with the surface potentials we will find from Lunar Prospector data in subsequent sections.

[5] Lunar surface charging is scientifically interesting in its own right, but even more so when we consider the charged lunar surface as one part of a coupled system. Solar plasma and photons also generate part of the tenuous lunar surface-boundary-exosphere [see, e.g., *Stern*, 1999]. The surface potential, which can affect the flux of charged particles to the surface, could therefore also influence the generation of some components of the exosphere. Furthermore, electric fields associated with lunar surface charging should affect the motion of pick-up ions—the ionized component of the lunar exosphere [*Hilchenbach et al.*, 1991, 1993; *Cladis et al.*, 1994; *Mall et al.*, 1998]. Finally, the same charging processes that affect the surface also influence individual dust grains. Electric fields repel like-charged dust grains from the charged surface, and if they can detach from the surface (which may require overcoming significant Van der Waals forces), electrostatic repulsion can levitate and/or transport some dust particles above the surface.

[6] The electrostatic transport of dust has been observed in the laboratory [*Doe et al.*, 1994; *Sickafoose et al.*, 2002] and modeled theoretically [*Nitter et al.*, 1998; *Nitter and Havnes*, 1992; *Stubbs et al.*, 2006, 2007c] and appears likely to occur on the Moon. There exists solid observational evidence for the electrostatic transport of dust within a few meters of the surface from a variety of sources, including Surveyor [*Rennilson and Criswell*, 1974] and the Apollo 17 Lunar Ejecta and Micrometeoroids (LEAM) surface experiment [*Berg et al.*, 1976; *Rhee et al.*, 1977]. Evidence for higher altitude dust (reaching to tens or hundreds of kilometers) from Apollo crew observations [*Criswell*, 1973; *McCoy and Criswell*, 1974], solar coronal photography [*McCoy*, 1976], and Clementine imagery [*Zook and McCoy*, 1991; *Zook et al.*, 1995] still remains more controversial.

[7] Both electric fields and dust could have potentially significant consequences for robotic and/or human lunar surface exploration. Spacecraft charging and discharge remains one of the leading causes of spacecraft failures in orbit [*Leach*, 1995; *Bedingfield et al.*, 1996; *Koons et al.*, 2000], and these effects could also prove significant on the lunar surface. Meanwhile, we cannot easily predict the extent of hazards to exploration from charged dust, but significant hazards could exist [*Stubbs et al.*, 2007a].

[8] In this paper, we present a reanalysis of selected Lunar Prospector (LP) data, for the first time self-consistently taking into account the floating potential of the spacecraft. This allows us to determine the lunar surface potential with much higher accuracy than previously possible. We can now determine the surface potential with sufficient fidelity to understand how the surface charges in response to incident currents in a wide variety of environments, including the solar wind, wake, terrestrial magnetospheric tail lobes, and plasma sheet, and during SEP events. In addition to characterizing the lunar electric field environment with unprecedented accuracy, we can for the first time place constraints on lunar photoemission and secondary emission efficiencies, allowing comparison to laboratory measurements and better understanding of how lunar regolith materials interact with photons and plasma in situ.

2. Previous Observations and Models of Lunar Surface Charging

2.1. Previous Surface Observations

[9] On the sunlit hemisphere of the Moon, the dominant charging current usually consists of photoelectrons ejected from the surface by solar UV radiation. Measurements by the Apollo 14 and 15 Suprathermal Ion Detector Experiment (SIDE) [*Hills et al.*, 1972] implied sunlit surface potentials in the solar wind on the order of 10 V [*Fenner et al.*, 1973; *Freeman et al.*, 1973; *Freeman and Ibrahim*, 1975], and *Goldstein* [1974] inferred potentials on the order of −3 to +5 V from Solar Wind Spectrometer measurements at the Apollo 12 and 15 sites. These data agreed roughly with

theoretical predictions, including those from *Singer and Walker* [1962], who showed that the sunlit surface should charge to a positive potential of ~20 V so that the incoming flux of electrons balances the small fraction of photoelectrons that overcome the potential drop across the sheath and escape. *Manka* [1973] performed similar calculations using probe theory and arrived at a surface potential estimate of ~9 V. Other investigators, using laboratory measurements of photoemission yields from lunar dust samples, inferred somewhat smaller positive potentials, around ~4 V [*Feuerbacher et al.*, 1972; *Willis et al.*, 1973].

[10] In the low-density geomagnetic tail lobes, photoelectron emission dominates even more thoroughly over ambient plasma currents, perhaps forcing the sunlit lunar surface to charge to even larger positive potentials. Measurements by the Apollo 14 Charged Particle Lunar Environment Experiment (CPLEE) [*O'Brien at al.*, 1971] were used to infer tail lobe potentials as high as +200 V in sunlight [*Reasoner and Burke*, 1972].

[11] On the night side of the Moon, on the other hand, in the absence of photoemission, currents from plasma electrons usually dominate, since electron and ion densities and temperatures are similar in most environments, but the lighter electrons move much faster and therefore contribute a much higher flux to the surface. In this environment, the lunar surface charges to a negative potential that repels most electrons, so that the smaller ion current can balance the remaining electron current. Before LP, no experimental data on nightside potentials existed, but measurements by SIDE near the terminator, where photoemission remains minimal due to the oblique incidence of solar UV radiation, indicated surface potentials of −50 to −100 V [*Freeman et al.*, 1972; *Lindeman et al.*, 1973; *Benson*, 1977]. These measurements agreed roughly with simple charging theory, which predicts an equilibrium negative potential in shadow on the order of a few times the electron temperature [*Whipple*, 1981; *Horányi*, 1996].

[12] However secondary electron emission can complicate matters by providing an effective source of positive current to the surface. Depending on incident electron energies, lunar secondary electron emission efficiencies can exceed unity [*Willis et al.*, 1973; *Horányi et al.*, 1998], in which case a shadowed surface can even charge positive. Theoretical predictions of nightside lunar potentials vary from 0 to −1800 V [*Manka*, 1973; *Knott*, 1973; *Freeman and Ibrahim*, 1975], depending on assumptions about plasma properties and secondary emission characteristics.

2.2. Previous Spacecraft Observations

[13] Unexpected Apollo subsatellite observations of electrons adiabatically reflected from crustal magnetic fields first led to the development of the electron reflectometry technique for mapping remanent magnetic fields [*Anderson et al.*, 1975]. Similarly, researchers serendipitously discovered the ability of electron reflectometry to determine surface electric fields. The LP Electron Reflectometer (ER) was designed to map lunar crustal magnetic fields but also found evidence for lunar electric fields from two different indicators.

[14] First, the loss cone angle was found to depend on energy. For adiabatic magnetic reflection, the cutoff pitch angle α_c (the angle between the initial electron velocity and the magnetic field beyond which electrons impact the lunar surface before reflecting) measured at the spacecraft is given by $\sin^2 \alpha_c = B_S / B_M$ (independent of energy), where B_S and B_M are magnetic field magnitudes at the spacecraft and the surface of the Moon. However LP observations in shadow in the geomagnetic tail lobes and solar wind wake instead revealed energy-dependent reflection [*Halekas et al.*, 2002]. The energy dependence of the loss cone clearly indicates the presence of electric fields, which modify the loss cone angle equation to read $\sin^2 \alpha_c = (B_S/B_M)\,(1 + e\Delta U/E)$, where E is the electron kinetic energy measured at the spacecraft and ΔU is the potential difference between the surface and the spacecraft. The observed loss cones fit this functional form [*Halekas et al.*, 2002]. In addition, a high-flux beam of electrons was often observed traveling upward along the magnetic field line from the surface. The upward-going electron beams have center energies corresponding to the inferred potential drop, indicating an origin as low-energy secondary electrons emitted from the surface and accelerated upward to the spacecraft through the potential drop [*Halekas et al.*, 2002].

[15] Initial LP ER measurements implied a potential drop between the spacecraft and the surface in shadow in the solar wind wake and geomagnetic tail lobes on the order of 30–50 V, suggesting negative nightside surface potentials of ~−125 V [*Halekas et al.*, 2002], though this estimate depended greatly on the then poorly constrained electrostatic charging properties of the LP spacecraft itself. Subsequent analyses of LP ER data primarily utilized the secondary electron beam as a diagnostic indicator of lunar surface charging and focused on times when the largest negative surface potentials occurred. When the Moon crossed the geomagnetic plasma sheet, LP found evidence for surface potentials as large as ~−1 kV, with these large negative potentials occasionally found even in sunlight [*Halekas et al.*, 2005a]. During SEP events, LP found evidence for even larger nightside potentials in the lunar wake, approaching ~−4 kV [*Halekas et al.*, 2007].

[16] Unfortunately, all previous analyses of LP ER data suffered from two crucial limitations. First, and most importantly, we did not know the floating potential of the LP spacecraft with respect to the ambient plasma. Since the ER technique actually senses the potential difference between the surface and the spacecraft, this implies that all previous LP estimates of the surface potential had a large and unknown offset. Second, all previous estimates have only used either the loss cone dependence or the secondary electron beam as an indicator of surface charging. The loss cone measurements focused on by *Halekas et al.* [2002] exploited already processed data previously utilized to infer surface crustal magnetic fields. These magnetic field studies routinely used energy channels as low as ~200 eV to determine the form of the loss cone, limiting the maximum measurable potential drop to ~100 V (since larger potential drops produce a secondary beam which begins to contaminate the loss cone at ~200 eV). Studies of larger potentials by *Halekas et al.* [2005a, 2007], meanwhile, only utilized the secondary electron beam. No investigation to date has self-consistently treated the entire measured electron distribution.

[17] We now present a new analysis of selected LP ER data, for the first time correcting for the spacecraft floating

potential, and self-consistently fitting to the entire electron distribution to determine the lunar surface electrostatic potential. Utilizing these new techniques, we can now present the first quantitative measurements from orbit of lunar surface electrostatic potentials.

3. Lunar Prospector Electron Reflectometer Data

[18] This study utilizes data from the LP ER to determine lunar electrostatic potentials. The ER was a top-hat electrostatic analyzer that measured full 3-D electron distribution functions (from 7–38 eV to 20 keV, covering all look directions). The analyzer had an intrinsic energy resolution of $\Delta E/E = \sim 0.25$, but the onboard processor summed adjacent energy bins together, resulting in an effective $\Delta E/E = \sim 0.5$. Though the ER made 3-D measurements with an 80-s cadence (corresponding to 120 km separation), the integration lasted only 2.5 s, ensuring an intrinsic spatial resolution for each individual measurement of only a few kilometers. We do not utilize higher cadence pitch angle sorted data in this study since we require full energy coverage not available at higher cadence. LP had a rapidly precessing polar orbit (~2 hr period), allowing full coverage of the lunar surface twice a month. LP orbited at ~100 km for the first year of the mission and at ~15–50 km for the second year of the mission. In its orbit around the Earth, the Moon spends ~75% of the time in the solar wind, and the rest in the terrestrial magnetosheath and geomagnetic tail (including tail lobes and plasma sheet). The LP mission returned ~18 months of data between January 1998 and July 1999, ensuring good coverage of the lunar surface in all relevant plasma environments, in a variety of different conditions, and over a full range of solar zenith angles.

4. Estimating the Lunar Prospector Spacecraft Potential

[19] Like the lunar surface, spacecraft charge in response to currents incident on their surface. This poses a constant problem for plasma measurements since the floating potential of the spacecraft shifts the energies of electrons and ions that reach the spacecraft. Researchers have used a variety of solutions to correct for the spacecraft potential, most based either on direct measurements of the spacecraft potential at the time of observation, or reconstruction of the spacecraft potential after the fact by requiring consistency of plasma measurements. For LP, this task proves particularly difficult since LP lacked both ion and electric field instruments. Furthermore, the lowest electron energy bin for the ER was centered at 7 eV or higher, and for much of the mission the lowest energy bin was centered at 38 eV.

4.1. Spacecraft Potential in Sunlight

[20] To determine the LP spacecraft potential in sunlight, we rely on measurements from the terrestrial magnetosphere in 1999, when the ER energy sweep extended down to 7 eV. At these times, we found that the ER energy coverage sufficed to measure both ambient plasma electrons and photoelectrons generated from the spacecraft (those not energetic enough to escape the photoelectron sheath around the spacecraft) and attracted back by the positive floating potential of the spacecraft relative to the plasma. We proceed by fitting the measured total electron distribution to the sum of a Maxwellian distribution representing the photoelectrons, of the form $f(v) = n \bullet (m/(2\pi kT))^{3/2} \exp[-mv^2/(2kT)$, and a kappa distribution representing the plasma electrons reaching the spacecraft, of the form:

$$f(v) = \frac{\Gamma(\kappa+1)}{(\pi\kappa)^{3/2}\Gamma(\kappa-1/2)} \frac{n}{\Theta^3} \left[1 + v^2/\left(\kappa\Theta^2\right)\right]^{-\kappa-1} \quad (1)$$

[21] For both of these distributions, n represents the density (zeroth velocity moment). For a Maxwellian, the temperature (proportional to the second velocity moment) is T, while for a kappa distribution the temperature $T_\kappa = \kappa / (\kappa - 3/2) * m\Theta^2/(2k)$, where Θ is the average thermal velocity. Both of these distributions can also be written in order to take into account a shift through a potential drop [see *Halekas et al.*, 2005b], allowing one to relate the distribution at the spacecraft to that outside the sheath. For a Maxwellian, this results in a distribution with a different effective density but the same temperature. For a kappa, this results in a distribution with different effective densities and temperatures but the same kappa index. In this case we are interested in the properties of the distribution at the spacecraft, so we model the distributions without a potential term.

[22] This two-component fit allows us to determine the total current to the spacecraft from plasma electrons by calculating the appropriate component of the first velocity moment of the kappa component of the fit and normalizing appropriately. Since the electron gyroradius greatly exceeds the spacecraft dimensions for all times of interest, we neglect the magnetic field. This current balances the escaping photoelectron current, if we neglect the small ion current (generally a safe assumption in sunlight). Our fitting procedure also determines the break between the photoelectron distribution and the plasma electron distribution, located where the electron energy equals the positive spacecraft potential with respect to the ambient plasma. By calculating these two crucial quantities, we determine the current–voltage curve of the spacecraft in sunlight (much like that of a Langmuir probe). We show a sample two-component fit in Figure 1, displaying the generally good quality of our fits. Note the importance of taking into account the low energy resolution of the ER—the fit before convolving the fitted distribution with the instrumental resolution appears rather poor, while a fit which takes into account instrumental resolution proves nearly indistinguishable from the actual data. Neglecting to take into account the instrumental resolution shifts the apparent break in the spectrum, resulting in a fit which can overestimate the spacecraft potential. Given the convolution with the instrumental resolution and the iterative nature of the fitting process, it proves difficult to calculate exact errors, but we estimate errors in the spacecraft potential of ~<10 V. We show the results of applying this same fitting procedure to many measurements in Figure 2 for a selected 12 hour period in the terrestrial magnetosphere.

[23] We fit the resulting current–voltage curve with a simple double exponential of the form $J = A * \exp(-U_{SC} / B) + C * \exp(-U_{SC}/ D)$, where $A = 1.07\ \mu A/m^2$, $B = 5$ V, $A = 0.016\ \mu A/m^2$, and $B = 60$ V. This resembles the functional form found by previous investigators for the Polar

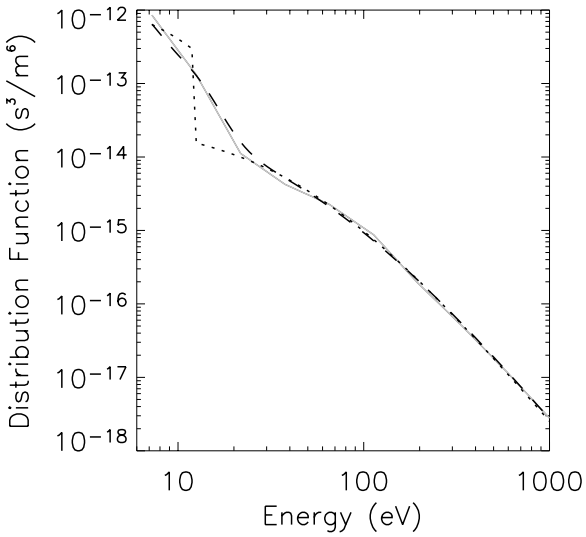

Figure 1. Typical distribution function observed in sunlight (light gray), measured at 14:39:50 on 29 April 1999, along with best fit distribution before (dotted) and after (dashed) convolving with the instrumental energy resolution. We find a plasma electron density of 0.4 cm^{-3}, an 88-eV temperature, and a spacecraft potential of +12 V.

[*Scudder et al.*, 2000], ISEE [*Escoubet et al.*, 1997], ISEE and GEOS [*Pederson*, 1995], and Voyager [*Scudder et al.*, 1981] spacecraft. As shown by comparing analogous fits from previous investigations (shown in Figure 2), the escaping photocurrent found for LP has a similar functional form but smaller magnitude than that for all but Voyager, which our results match very well.

[24] With the current–voltage curve determined above, we can now routinely determine spacecraft potential in sunlight (assuming the photoelectron yield of the spacecraft remains relatively constant), even when the energy sweep only extends down to 38 eV. We accomplish this by fitting the measured electron spectrum (being careful to exclude any secondary or photoelectron population at low energies) to a kappa distribution. The escaping photocurrent is then approximated by integrating over the fitted electron distribution (thereby determining the electron current to the spacecraft, which balances the escaping photocurrent), and we find the corresponding spacecraft potential from the current–voltage curve determined above. With the spacecraft potential in hand, we can then correct measured electron spectra by shifting appropriately in energy, allowing us to determine the actual plasma parameters, uncontaminated by the effects of spacecraft charging.

4.2. Spacecraft Potential in Shadow

[25] Unfortunately, determining the LP spacecraft potential in shadow proves a much more difficult task. In shadow, with photoemission absent, the spacecraft will generally charge negative. Rather than attracting electrons to the spacecraft, a negative potential instead repels electrons, reducing the portion of the distribution that we measure. Furthermore, any secondary population escapes the spacecraft rather than forming a break in the distribution that we can measure. Without measurements of ions, we cannot use a technique analogous to that described above. Therefore we rely on a different method to correct for spacecraft potential in shadow.

[26] The spacecraft in shadow will reach an equilibrium potential found by balancing the incident electron current with the secondary electron emission current and the incident ion current. The secondary emission efficiency depends on incident electron energy in a manner that we can approximate using the Sternglass formula $\delta(E) = 7.4\delta_m E/E_m \bullet \exp(-2\sqrt{E/E_m})$ [*Sternglass*, 1954]. Using this formula, we can calculate the total secondary electron current by integrating this formula over the incident electron spectrum, with appropriate limits. As long as we know the incident electron and ion currents, the electron spectrum, and the spacecraft secondary emission parameters, we can then in principle calculate the spacecraft potential.

[27] Utilizing this prescription, we can construct a charging model for the LP spacecraft in shadow. We calculate electron, ion, and secondary emission currents as a function of spacecraft potential and balance them to determine the resulting floating spacecraft potential with respect to the ambient plasma. In practice, we calculate the electron current by measuring the electron spectrum and fitting to a kappa distribution. We do not know the ion spectrum, but as a first approximation we assume a kappa function with the same kappa parameter and ion densities and temperatures equal to electron densities and temperatures. The ion current represents the smallest term in the equation, so this approximation usually does not affect the results significantly. We further assume nonflowing plasma—usually a good approximation in shadow, where the LP spacecraft lies either in the lunar wake or terrestrial magnetosphere. Significant flows could exist in the plasma sheet, which might prove important for the ion currents but which should still not contribute significantly compared to thermal motion for electrons. We utilize the thick sheath approximation (as

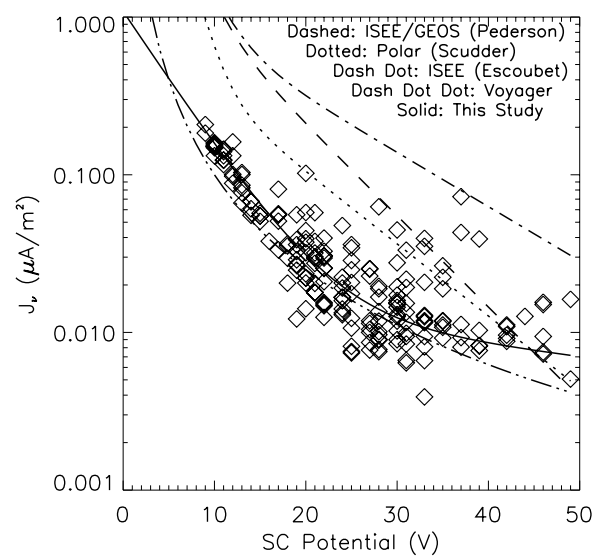

Figure 2. Escaping photoemission current as a function of positive spacecraft potential from a series of orbits in the terrestrial magnetosphere on 29 April 1999, with best fit and similar fits from analogous studies performed by other authors for other spacecraft.

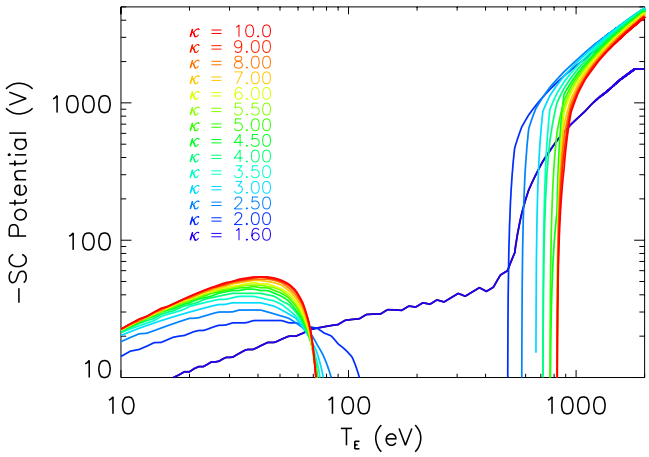

Figure 3. Magnitude of negative spacecraft potential as a function of electron temperature, calculated assuming kappa function electron and ion distributions, with secondary yield estimated according to the Sternglass formula with E_m = 500 eV and δ_m = 1.5 for various values of κ.

in *Horányi* [1996]) since the sheath exceeds the size of the spacecraft, ensuring that ion current to the spacecraft increases as a function of negative spacecraft voltage as more ions are drawn through the sheath to the spacecraft.

[28] One further subtlety lies in the fact that we do not measure the ambient electron distribution, but that distribution shifted through the potential drop to the spacecraft. Luckily, we can utilize the properties of the kappa function distribution to relate our kappa fit (and the corresponding density and temperature) of the electron spectrum measured at the spacecraft to a kappa distribution with the same kappa parameter (but different density and temperature), representing the electron spectrum outside the sheath. In particular, we can relate the uncorrected electron temperature T_{uc} measured at the spacecraft to the correct electron temperature T_c outside the sheath and the spacecraft potential U_{SC} by $kT_c = kT_{uc} + eU_{SC} / (\kappa - 3/2)$ [*Halekas et al.*, 2005b]. In addition, we can relate T_c to U_{SC} using the charging model described above. Utilizing these two relations together, we obtain a transcendental equation which we can solve numerically for the spacecraft potential.

[29] Unfortunately, we do not know the secondary emission properties of the LP spacecraft a priori, so we cannot yet complete the model described above. One could approximate these parameters by constructing a model of the LP spacecraft and utilizing the known secondary emission properties of each constituent material. A comprehensive study of Freja spacecraft charging successfully utilized this approach [*Eriksson et al.*, 1998]. However, another in depth study, addressing the charging of LANL satellites, found that the average secondary emission properties did not match those of any of the constituent materials [*Davis et al.*, 2003]. We elected to search through a reasonable range of secondary emission characteristics to find those which best satisfied a metric described below. The resulting best fit secondary emission parameters do not necessarily reproduce those of any of the materials composing the LP spacecraft as measured on the ground but rather form the best representation of the average charging properties of the LP spacecraft in orbit.

[30] In the terrestrial magnetotail lobes, plasma conditions generally remain quiet and nonturbulent. In addition, the magnetic field is steady and roughly aligned with the Moon–Sun line or equivalently the Earth–Moon line. In this environment, we observe few rapid discontinuities in electron fluxes. When we cross the boundary between the portion of the orbit where the spacecraft receives illumination and that where the spacecraft lies in shadow (at a solar zenith angle of ~100–110°), however, we can observe real discontinuities in the electron fluxes. In particular, we will generally observe only Earthward-going fluxes in shadow since the Moon blocks tailward-going fluxes in this region. However, if we look only at Earthward-going fluxes, we obtain a quantity which should have no real discontinuities at the light/shadow boundary—measured discontinuities in Earthward-going flux at the light/shadow boundary must therefore result purely from spacecraft charging. Therefore, by searching for the spacecraft charging model which best eliminates any artificial discontinuities in the Earthward-going electron flux at light/shadow boundaries in the tail lobes, we can tune the spacecraft charging model to find the secondary emission characteristics of the spacecraft.

[31] To calculate the best fit secondary emission properties for LP, we therefore utilized data from a number of tail lobe passes and calculated the resulting negative spacecraft potential (using the model described above) in shadow for a range of reasonable secondary emission properties (δ_m = 0.75–2.0, E_m = 200–800 eV). In sunlight, meanwhile, we used the prescription described in the previous section to find the positive spacecraft potential. We then used these calculated spacecraft potentials for both sunlight and shadow to correct the measured electron energies and searched through all of the range of possibilities to find best fit secondary emission parameters, that is, those which most successfully reduced all artificial discontinuities in Earthward-going electron fluxes at light/shadow boundaries, of δ_m = 1.5, E_m = 500 eV.

[32] We show the predicted behavior of the LP spacecraft potential in shadow as a function of electron temperature and kappa parameter, utilizing these best fit secondary emission parameters, in Figure 3. We find that the spacecraft charges negative until kT/e reaches 60–100 eV (depending on κ), whereupon the total integrated secondary emission plus the incident ion flux becomes large enough to balance the incident electron flux. At this point, in our model, the spacecraft potential becomes identically zero. In fact, it will charge slightly positive in order to return secondary electrons to the spacecraft (analogous to the situation in sunlight with photoelectrons). However the secondary electron temperature should not exceed a few eV [*Whipple*, 1981], so this positive potential should remain near zero. At electron temperatures of a few hundred to a thousand eV (depending on κ), the integrated secondary emission drops enough that the spacecraft again can again charge negative. Note that for a kappa parameter of 1.6, the potential remains negative for all electron temperatures. We must understand that the kappa distribution remains strictly valid only for $\kappa > 1.5$, with smaller kappa parameters producing a distribution for which the second velocity moment (temperature) integral does not converge. A kappa parameter of 1.6 lies so near

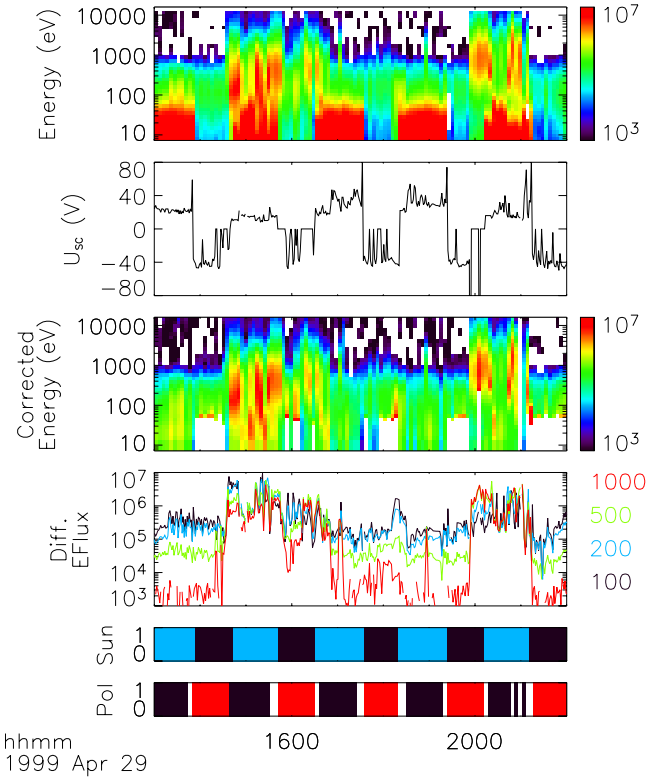

Figure 4. Data from a series of orbits in the terrestrial magnetosphere on April 29 1999, showing uncorrected Earthward-going electron differential energy flux, calculated spacecraft potential, corrected Earthward-going differential energy flux in both spectrogram and line plot formats, and color bars showing spacecraft illumination (black = shadow, blue = sun) and magnetic connection to the surface (red = positive polarity, black = negative polarity).

this critical value that the resulting distribution closely approximates a power law and possesses a high energy component that contributes very significantly to the integral. In practice, we seldom observe electron distributions with kappa parameters less than 2.

4.3. Caveats

[33] At some times, in both sunlight and shadow, measured electron fluxes suddenly increase at the lowest energies, even when we remove the photoelectron component in sunlight. This could imply the presence of an additional secondary population, or it could imply that the electron distribution has two components, with the lower component barely resolved by the ER. When this occurs in the plasma sheet, we generally fit to the higher component and neglect this lower energy population. We assume that this low energy population corresponds to a secondary population generated at the spacecraft. In the solar wind, on the other hand, this low energy population likely corresponds to the solar wind core, and we always fit to the lowest energy component we can resolve (while still removing the photoelectron component) in order to ensure that we fit to the solar wind core, rather than a halo population. We have found that this prescription generates the most reasonable results in both cases. However the possibility exists that we may miss an important low energy plasma electron population at times due to the limited low energy coverage of the LP ER.

4.4. Corrected Data

[34] We now have a prescription for correcting LP ER data for the effects of spacecraft potential in both sunlight and shadow. We show the result for a series of orbits in the terrestrial magnetotail lobes and plasma sheet in Figure 4. The uncorrected Earthward-going fluxes shown in the top panel have clear discontinuities at light/shadow boundaries, and we observe a very significant photoelectron population which completely swamps any real plasma electron population below ~50 eV in sunlight. Corrected Earthward-going fluxes (shifted appropriately in energy according to the calculated spacecraft potential) no longer show any sign of artificial discontinuities at light/shadow boundaries. Flux discontinuities still occur, but only associated with transitions between tail lobe and plasma sheet (e.g., at 14:30, 19:50, and 21:15) or magnetic connection boundaries (e.g., at 18:20 and 19:15). The calculated spacecraft floating potential generally remains between ±50 V, with positive excursions from this range for very low density regions in sunlight, and negative excursions from this range for very high temperature electron populations in shadow.

[35] Correcting for spacecraft potential allows us for the first time to accurately determine the lunar surface electrostatic potential with no arbitrary offsets. In addition, we can determine downward-going electron density and temperature, corrected for the effects of spacecraft potential, allowing the best possible characterization of how the lunar surface responds to incident currents.

5. Determining the Lunar Surface Potential

5.1. Technique

[36] The determination of spacecraft potential described in the preceding sections constitutes our first advance in determining lunar surface potentials. This allows us to determine the lunar surface potential with no arbitrary offsets. In addition, we have developed a more sophisticated scheme to self-consistently fit to the entire measured electron distribution and determine the lunar surface potential with the greatest possible fidelity.

[37] Outside of the plasma sheath around the LP spacecraft, we can describe the electron loss cone angle by the equation $\sin^2 \alpha_c = (B_S/B_M)(1 + eU_M/E)$, with U_M the lunar surface potential, and B_S/B_M the ratio of the magnetic field at the spacecraft to that at the surface. This equation describes the boundary between electrons adiabatically reflected by combined magnetic and electrostatic forces, and those lost by impact with the surface. This equation necessarily approximates electron motion as fully adiabatic. In fact, since lunar electric and magnetic field scales do not in general greatly exceed the electron gyroradii, we can only consider electron motion quasi-adiabatic at best. Previous investigations have shown the importance of the nonadiabatic nature of electron motion near the lunar surface at times, especially for magnetic field lines intersecting the surface at oblique angles, producing a "tip-angle effect" [*Halekas et al.*, 2003]. However the assumption of adiabatic motion still represents a very good first approximation to

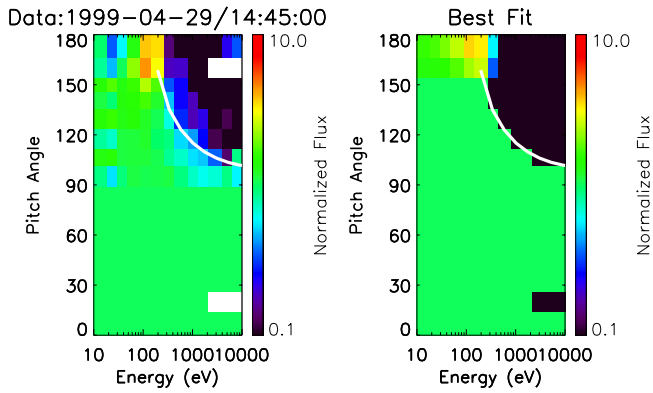

Figure 5. Normalized energy pitch angle distribution measured at 14:45 UT on 29 April 1999, with best fit synthetic distribution (on right) from automated surface potential determination. The best fit uses the spacecraft potential $U_{SC} = 11$ V and finds that the lunar surface potential $U_M = -160$ V and the magnetic field ratio $B_S/B_M = 0.975$.

electron reflection from lunar surface electric and magnetic fields. Meanwhile, electric fields near the lunar surface also accelerate a secondary electron beam generated locally at low energies up to the spacecraft, producing an upward-going beam with a center energy corresponding to the lunar surface potential [*Halekas et al.*, 2002]. The final electron distribution consists of a superposition of the loss cone distribution and this secondary beam.

[38] Unfortunately, we do not measure this distribution directly; instead, we measure the distribution at the spacecraft after it has passed through the spacecraft's plasma sheath. The secondary beam simply shifts in energy according to the spacecraft potential (for a large negative spacecraft potential, the secondary beam may not reach the spacecraft—we take this into account in our analysis). The loss cone angle, on the other hand, could change in a more complicated manner. If electrons behave fully adiabatically around the spacecraft, we should replace U_M with $\Delta U = U_M - U_{SC}$ in the loss cone equation. On the other hand, if electrons conserve their pitch angle, but merely shift in energy as they go through the sheath to the spacecraft, we should instead replace E with $E - U_{SC}$ in the loss cone equation. Since the relevant electron gyroradii generally greatly exceed the spacecraft sheath dimensions, we adopt the second approach. Simple particle tracing simulations show that this approximation should generally remain valid for reasonable parameters. In any case, either equation has the same asymptotes for the curved loss cone, with only a small change in the shape of the curve, so using either equation will give approximately the same results for the lunar surface potential. Since the measurement of the secondary beam energy has no such complications, it therefore provides perhaps the best marker of the lunar potential.

[39] We proceed to fit to the measured electron distribution to determine the lunar surface potential. We begin by normalizing the distribution by dividing both reflected and incident halves of the distribution by the incident half, so that we fit the ratio of reflected to incident flux. We then create a synthetic distribution with a loss cone angle corresponding to the equation (in accordance with the discussion above):

$$\sin^2 \alpha_c = B_S/B_M \bullet (1 + eU_M/(E - U_{SC})) \qquad (2)$$

[40] To this distribution, we add an upward-going beam, centered at an electron energy of $U_M - U_{SC}$. We then calculate a least squares fit parameter for the entire distribution using the logarithms of the synthetic and measured fluxes. We repeat this procedure for a full range of magnetic ratios and lunar surface potentials to find the best fit to the measured electron distribution.

[41] We show a typical example of a fit to a measured distribution in the terrestrial plasma sheet in Figure 5. For this case, we find a best fit synthetic distribution with a very good match to both the secondary beam and the energy-dependent loss cone angle. The measured loss cone and beam do not appear quite as sharp as the synthetic case. A cut through the loss cone at a constant energy would find a modest slope to the loss cone rather than the sharp step function of the synthetic distribution. This slight broadening of the loss cone could result from slightly nongyrotropic electron behavior resulting from passage through the spacecraft sheath. Alternatively, it may result from waves, which generally act to smooth out discontinuities in a distribution function. Nevertheless, the fit still finds the right average loss cone angle and functional dependence on energy (consistent with the energy of the secondary beam), and therefore the correct lunar surface potential.

5.2. Limitations

[42] Our potential determination technique works very well for negative lunar surface potentials. Since both magnetic fields and negative electrostatic potentials reflect electrons, we can easily utilize the energy dependence of the reflection to determine both parameters. In addition, for negative potentials, the secondary beam provides an excellent marker of the surface potential.

[43] Unfortunately, our technique does not work well for positive lunar surface potentials. Since magnetic fields reflect electrons, but positive electric fields attract them, positive surface potentials in essence produce a nonmonotonic potential (a superposition of a magnetic mirror potential and an electrostatic potential), which depends on the initial electron energy and pitch angle. The loss cone angle equation still works mathematically for a positive electrostatic surface potential. However, in practice, one can only determine an attractive electrostatic potential if another force can subsequently reflect the electrons before they impact the surface. If the crustal magnetic fields responsible for reflecting electrons had an effective scale height much smaller than the photoelectron sheath scale height (so that magnetic fields could still reflect electrons after they passed through most of the photoelectron sheath), one could determine a positive lunar surface electrostatic potential utilizing electron reflectometry. Unfortunately, however, the expected positive electric field scale height (photoelectron sheath thickness) of a few meters on the dayside ensures that we cannot in general utilize electron reflectometry to determine positive surface potentials. With an ion instrument, one could use ion reflectometry to sense posi-

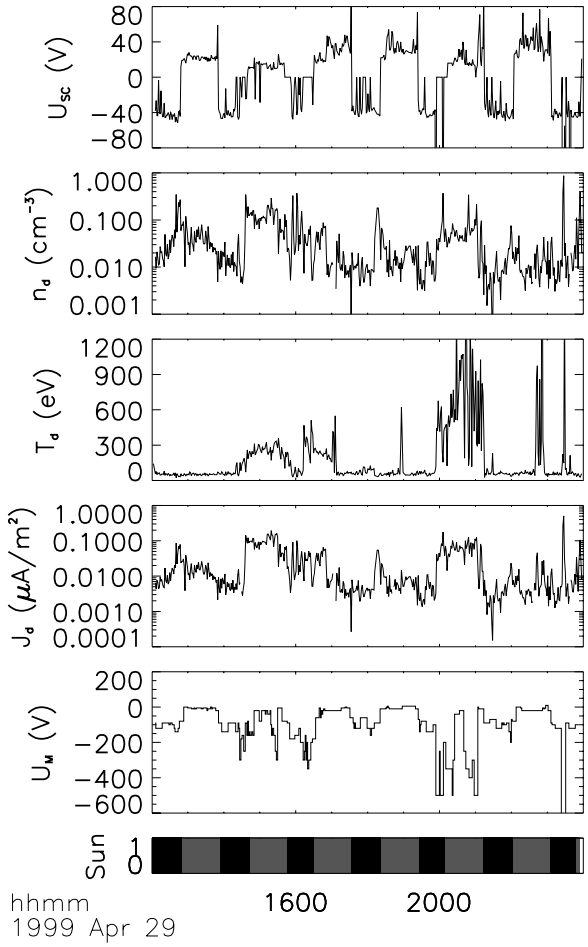

Figure 6. Calculated spacecraft potential, corrected downward-going electron density, temperature, and current, lunar surface potential, and color bar showing spacecraft illumination (black = shadow, gray = sun) for a series of orbits in the terrestrial magnetosphere on 29 April 1999.

tive potentials (though the larger ion gyroradius would decrease the surface resolution of the technique), but we cannot employ this solution on LP, which only had an electron instrument.

[44] Our fitting procedure does occasionally find small positive surface potentials. However we consider such determinations invalid, merely showing the intrinsic error of our fitting technique. Indeed, given the energy resolution and coverage and the pitch angle resolution of the ER, we estimate that, in most cases, we cannot clearly distinguish surface potentials smaller than 20 V from zero potential.

6. Lunar Surface Potential in the Earth's Magnetosphere

[45] We show our first results in Figure 6 for a series of orbits through the terrestrial magnetosphere on 29 April 29 1999, during a period including both tail lobe and plasma sheet encounters. We calculate the spacecraft potential by utilizing the procedures outlined in section 4. Using the spacecraft potential, we can then shift the measured electron distribution appropriately in energy, enabling the calculation of the correct density, temperature, and current (as calculated from the kappa distribution, using the formula $J_\kappa = nq\sqrt{kT_\kappa/(2\pi m)}\sqrt{\kappa - 3/2} \bullet \Gamma(\kappa - 1)/\Gamma(\kappa - 1/2)$) of the downward-going electrons that contribute to the lunar surface charging. We then calculate the lunar surface potential by utilizing the procedures outlined in section 5. To ensure the highest quality measurements, we hand check every step of this process. For most of the time period in question, we find a negative lunar surface potential on the night side and a potential statistically indistinguishable from zero on the day side. However, for very energetic plasma sheet encounters, we find some negative lunar surface charging events even in sunlight (e.g., 15:20–15:30 and 20:35–21:00) in agreement with previous results from *Halekas et al.* [2005a]. For the first time, we can clearly see that the magnitude of the lunar surface potential depends directly on downward-going electron temperature. We could not make this association with the uncorrected data used in previous studies [*Halekas et al.*, 2002] since spacecraft charging significantly affected both estimates of lunar surface potential and estimates of downward-going electron temperature.

[46] In Figure 7, we show the magnitude of the negative lunar surface potential determined by our fitting procedure, as a function of the solar zenith angle (SZA) of the foot point (the point on the lunar surface magnetically connected to the LP spacecraft). We find that the lunar nightside generally floats around a potential of ~ -100 V in the tail lobes (points with low electron temperatures) and increases to several hundred volts to nearly a kilovolt negative in the plasma sheet (points with high electron temperatures). On the dayside in the tail lobes, meanwhile, surface potentials remain smaller than 20 V (statistically indistinguishable from zero), with the transition between negative potentials and small unmeasurable potentials occurring very close to the terminator. Finally, even on the day side, we find that surface potentials can reach several hundred volts negative in the plasma sheet, even well forward of the terminator.

[47] On the day side in the terrestrial magnetosphere, the electron current incident on the lunar surface should balance the escaping photocurrent (with ion current providing a negligible contribution). Secondary currents could also prove important, but generally remain smaller than photocurrents. In Figure 8, we plot the magnitude of the negative lunar dayside surface potential against the electron current incident on the lunar surface, normalized by the cosine of the SZA (to correct for the oblique incidence of sunlight at higher SZA). The transition between small unmeasurable potentials and large negative potentials should occur when the incident electron current balances the entire photocurrent. Our data suggest that this occurs at an incident SZA-normalized current of ~ 0.1 μA/m^2 (presumably equal to the total photocurrent). However published laboratory data suggests a total photocurrent from the lunar surface of ~ 4.5 μA/m^2, almost two orders of magnitude larger [*Feuerbacher et al.*, 1972; *Willis et al.*, 1973]. This discrepancy either implies lunar photoemission in situ much smaller than predicted from laboratory experiments, a drastic underestimation of the incident electron current, or some unexpected charging mechanism. Both plasma ions and secondary electron emission contribute positive currents to the surface, so accounting for these currents would only make the discrepancy worse.

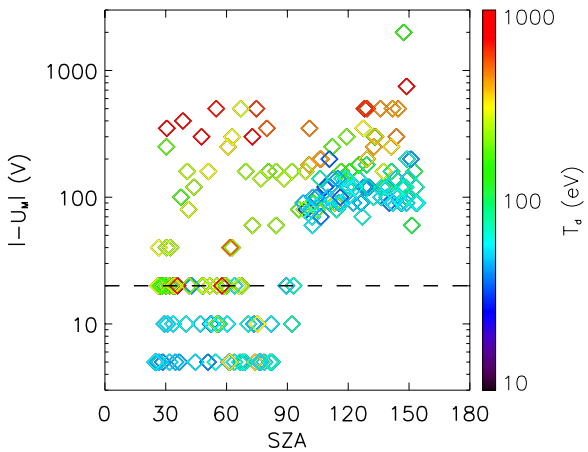

Figure 7. Magnitude of negative lunar surface potentials observed in the terrestrial magnetosphere during the time period shown in Figure 6, as a function of foot point solar zenith angle (SZA), colored according to the log of the downward-going electron temperature. Dashed line shows approximate measurement threshold.

[48] We consider it extremely unlikely that we could have underestimated the incident electron current by two orders of magnitude, especially since during this time period the ER energy sweep extends down to 7 eV, making a significant unmeasured low energy electron population unlikely. In addition, the more directly data-based determination of spacecraft potential in sunlight makes a large discrepancy due to poor estimation of the spacecraft potential unlikely. In any case, we note that the low current value we derived proves relatively insensitive to any of the processing which we have applied to the data, including the spacecraft potential correction. Indeed, an earlier analysis, using completely uncorrected data, suggested a similar result [*Halekas et al.*, 2005a]. Therefore this result appears robust and if taken at face value implies in situ photoemission from the lunar regolith orders of magnitude smaller than that predicted from laboratory experiments.

[49] Alternatively, some theoretical work suggests the possibility of nonmonotonic solutions for the electrostatic potential distribution in the sheath above the lunar surface [*Guernsey and Fu*, 1970; *Fu*, 1971; *Nitter et al.*, 1998], which could potentially explain this surprising discrepancy. In this case, the potential near the surface, rather than varying monotonically from the surface through the sheath, would decrease from the value at the surface (theoretically either positive or negative, but in this case presumably negative, since we see a secondary electron beam) to a local minimum before increasing to the ambient value above the sheath. This very different potential variation results from only a slightly different space charge distribution. The charge distribution and associated potential minimum acts to trap photoelectrons generated at the surface (as well as reflecting some incident plasma electrons), allowing the surface potential to assume very different values from those predicted by a more typical calculation for the monotonic potential case. If such a nonmonotonic potential distribution existed above the lunar surface, our reflectometry technique would then sense the negative potential at this minimum (on the order of the plasma electron temperature [*Fu*, 1971]) rather than the potential of the surface. The potential of the surface must not differ greatly from the value at the potential minimum since we still see a reasonably consistent secondary electron beam, but since the difference between the two potentials need only suffice to trap most of the photoelectron distribution (a low-temperature population) below the potential minimum, this seems possible. Surprisingly, some work suggests that such a nonmonotonic potential distribution could even prove more energetically stable than the usual monotonic distribution in many cases [*Guernsey and Fu*, 1970; *Fu*, 1971; *Nitter et al.*, 1998]. If so, even the small negative potentials on the dayside in the tail lobes often indicated from our analysis might prove real, though our measurements probably cannot reliably resolve such small potentials. However it remains unclear whether this type of space charge distribution could persist in the real lunar environment, when taking into account the actual input currents and the time history of the surface charging.

[50] On the nightside, in the absence of photoemission, we similarly attempt to constrain lunar secondary emission efficiencies. We plot the magnitude of the negative nightside lunar potential against the temperature of the downward-going electrons (as determined from corrected LP data) in Figure 9. In shadow, surface charging should depend directly on electron temperature, and indeed we observe a clear dependence of the lunar surface potential on electron temperature. Charging also depends on the kappa parameter of the distribution, possibly leading to some of the observed scatter. We find negative charging for the full range of measured downward-going electron temperatures, which places strong constraints on the lunar secondary emission yield.

[51] We calculate several representative predictions for lunar surface potential as a function of electron temperature. To accomplish this, we use exactly the same code that we use to calculate the LP spacecraft charging in shadow (as described in section 4.2). However, instead of the thick sheath approximation used for the spacecraft, we use a thin sheath approximation appropriate for the Moon since the ion current to the surface should not increase as a function of the negative surface potential (since the plasma sheath scale height remains always too small relative to the size of the Moon to draw in significant extra current through the

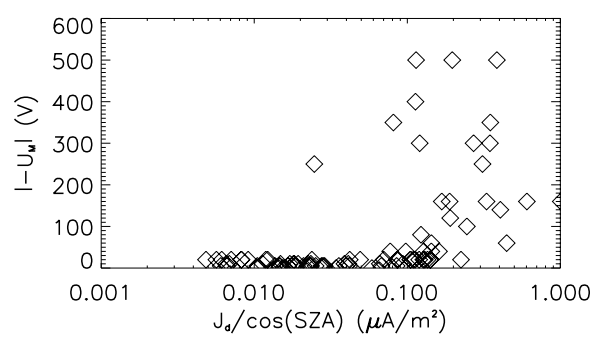

Figure 8. Magnitude of negative dayside lunar potentials observed in the terrestrial magnetosphere during the time period shown in Figure 6 as a function of downward-going electron current normalized by the cosine of the SZA.

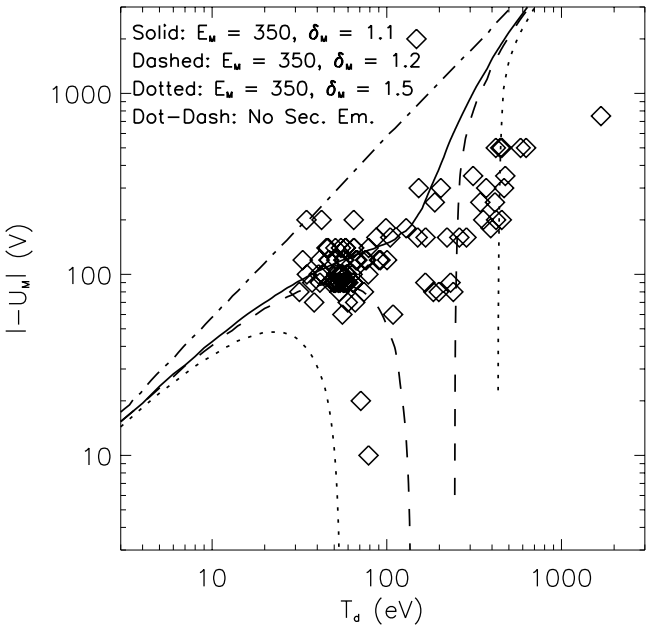

Figure 9. Magnitude of negative nightside lunar surface potentials observed in the terrestrial magnetosphere during the time period shown in Figure 6 as a function of downward-going electron temperature, with representative fits.

sheath). We note that this difference ensures that the lunar surface charges to a more negative value than the LP spacecraft as observed. Using this model, for an average kappa parameter of 4.5, we calculate secondary emission for E_m = 350 eV, and several different δ_M. The 350-eV value is consistent with those measured in the laboratory [*Willis et al.*, 1973; *Horányi et al.*, 1998]. However laboratory experiments found a δ_M of ~1.5 for normal incidence or ~3.0 for isotropic incidence. The value for isotropic incidence should more closely approximate electron incidence on the lunar surface, but neither of these values can successfully reproduce the observed charging behavior, as demonstrated in Figure 9. Even for δ_M = 1.5, the range over which the surface does not charge negative extends from electron temperatures of 50 to 500 eV, clearly not in agreement with data (errors in electron temperature determination could be consistent with a small "hole" in the charging, but not one extending over this range in temperatures). A model with no secondary emission also does not fit our data, as expected. Instead, a model with δ_M = 1.1–1.2 fits the observed data best, successfully reproducing the inflection point in the potential curve, though still overestimating surface potentials for the largest temperatures (we note that this overestimation could result due to our assumption of equal electron and ion temperatures—in fact, in the plasma sheet at lunar distances, where we observe these higher temperatures, the ion temperature likely significantly exceeds the electron temperature [*Rich et al.*, 1973], which would act to decrease the magnitude of negative surface charging). Observations therefore suggest somewhat smaller secondary emission currents from the lunar regolith in situ than previously measured in the laboratory.

[52] The lower photoemission and secondary emission efficiencies from lunar regolith materials in situ implied by our measurements, if real and not due to some other effect like nonmonotonic potential variation with altitude, may occur due to scattering in uneven surface regolith materials, resulting in less electron escape from the surface. Alternatively, the material properties of the top layer of lunar fines, constantly exposed to solar wind bombardment on the surface may differ slightly from those of samples measured in the laboratory. Finally, secondary emission and photoemission in situ in the tenuous near-vacuum plasma environment of the Moon may simply operate differently than they do in the laboratory environment (where, for example microlayers of atmospheric gases may affect the results).

7. Lunar Surface Potential in the Solar Wind and Lunar Wake

[53] We now move on to consider the lunar surface potential in other environments encountered by the Moon. First, we investigate a series of orbits in the solar wind and lunar plasma wake on 23 March 1998. We calculate the

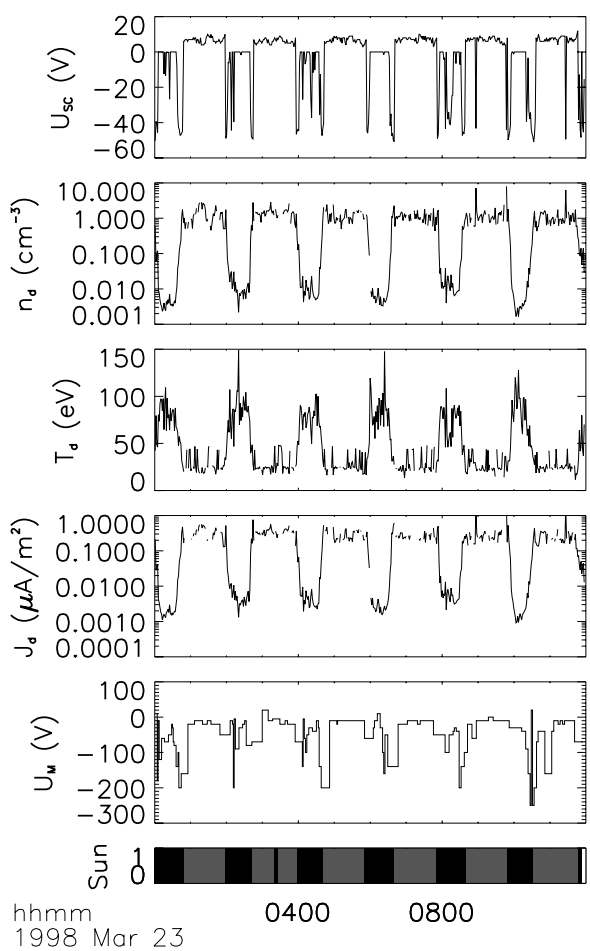

Figure 10. Calculated spacecraft potential, corrected downward-going electron density, temperature, and current, lunar surface potential, and color bar showing spacecraft illumination (black = shadow, gray = sun) for a series of orbits in the solar wind and lunar wake on 23 March 1998.

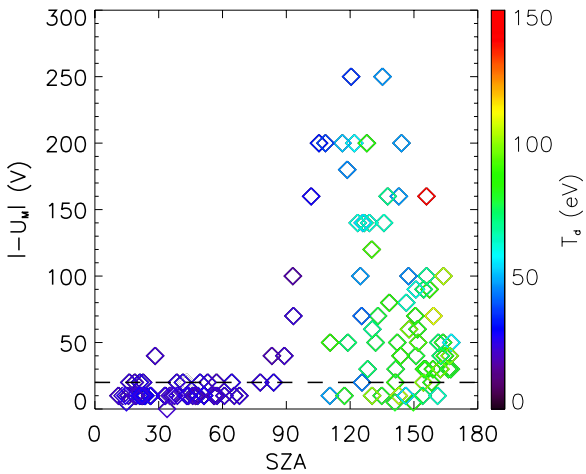

Figure 11. Magnitude of negative lunar surface potentials observed in the solar wind and lunar wake during the time period shown in Figure 10, as a function of foot point SZA, colored according to the magnitude of the downward-going electron temperature. Dashed line shows approximate measurement threshold.

spacecraft potential, downward-going electron density, temperature, and current and lunar surface potential just as we did for the magnetospheric case in the previous section (with the same level of quality control) and display the results in Figure 10. The electron density drops by 2–3 orders of magnitude in the lunar wake, and the temperature increases by almost an order of magnitude. This occurs due to velocity filtration of a non-Maxwellian solar wind electron distribution (only the high-energy tail of the distribution can overcome the ambipolar potential across the wake boundary), as described in detail in *Halekas et al.* [2005b]. The spacecraft potential goes negative at the edges of the wake as expected, but due to the significant temperature increase in the central wake, it actually returns to a near-zero value in the central wake due to the increase in secondary emission from the spacecraft with increasing electron temperature. We note that the lunar surface potential seems to follow a similar pattern, with the most negative surface potentials found near the edge of the wake rather than in the central portion. We must emphasize that the lunar surface potential shown here is referenced relative to the local wake plasma, not the solar wind. Due to the ambipolar potential drop across the wake boundary, which forms to slow the lighter and faster electrons relative to the more massive and slower ions and maintain quasi-neutrality as solar wind plasma fills in the lunar wake [*Samir et al.*, 1983; *Halekas et al.*, 2005b; *Farrell et al.*, 2008], the potential drop between the undisturbed solar wind and the lunar surface greatly exceeds that between the wake plasma and the lunar surface (shown here).

[54] In Figure 11 we show the magnitude of the negative lunar surface potential as a function of the SZA of the foot point (just as in Figure 7 for the magnetospheric observations). As expected, over most of the day side, surface potentials remain statistically indistinguishable from zero. At SZA of 75–90° (in rough agreement with theoretical predictions and previous measurements [*Manka*, 1973; *Stubbs et al.*, 2007b; *Benson*, 1977]), the lunar surface potential begins to go measurably negative, as electron currents start to exceed the sum of the ion and photoelectron currents (both reduced by oblique incidence at high SZA). The surface potential rises steeply as we cross the terminator and enter the lunar wake, but as we travel further into the lunar wake, the electron temperature rises continuously and the surface potential peaks at a few hundred volts negative and then falls back to smaller magnitudes ($|U_M| < 100$ V) in the central wake. This may happen because, analogous to the spacecraft case, secondary emission increases with increasing electron temperature, finally choking off the negative charging and returning the surface to a near-zero potential with respect to the ambient plasma. This represents the first clear observation of this intriguing lunar charging behavior, though earlier observations suggested something similar [*Halekas et al.*, 2002].

[55] We plot the magnitude of the negative nightside lunar surface potential in the lunar wake against downward-going electron temperature in Figure 12 (as we did in Figure 9 for the magnetospheric observations). We also show several representative models of the lunar surface potential, using the same charging model developed previously (again utilizing a thin sheath approximation appropriate for lunar surface charging). As before, the data seem reasonably consistent with a model with $E_m = 350$ eV, $\delta_M = 1.1–1.2$. However, in the wake, unlike in the terrestrial magnetosphere, we do find clear evidence for a "hole" in the charging, as the magnitude of the surface potential actually decreases to near zero at electron temperatures of ~100 eV, more consistent with a δ_M of 1.2 than 1.1. Unfortunately, we do not encounter high enough temper-

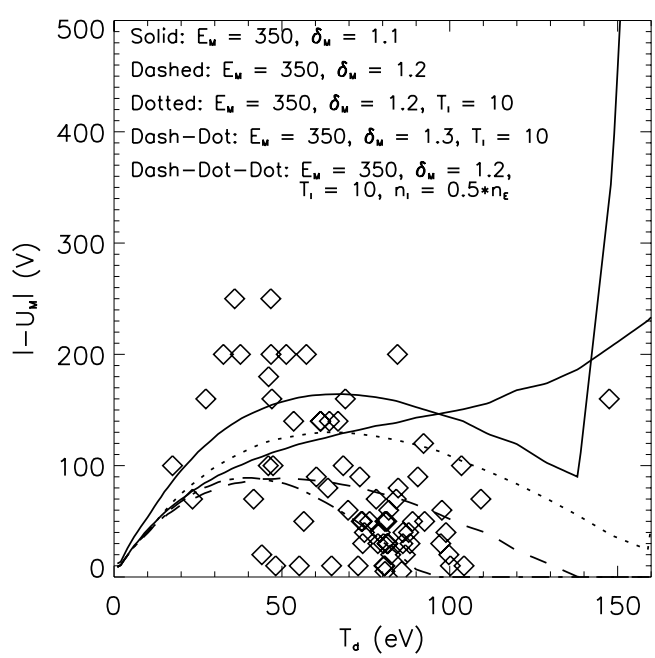

Figure 12. Magnitude of negative nightside lunar surface potentials observed in the lunar wake during the time period shown in Figure 10, as a function of downward-going electron temperature, with representative fits.

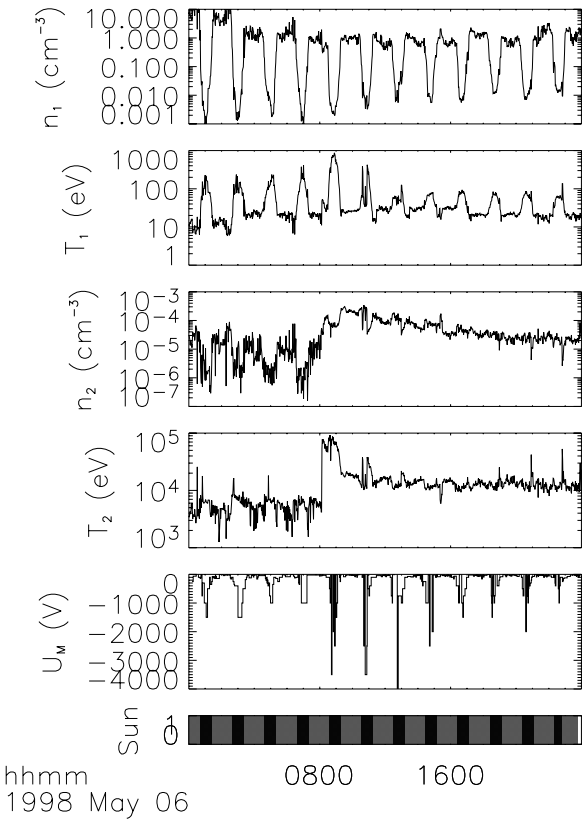

Figure 13. Downward-going electron density and temperature (two components each), lunar surface potential, and color bar showing spacecraft illumination (black = shadow, gray = sun) for a series of orbits in the solar wind and lunar wake during a solar energetic particle (SEP) event on 6 May 1998.

atures in the lunar wake to find out at what electron temperature negative charging resumes and thereby determine the width of the "hole", i.e., the temperature range where the surface potential goes slightly positive instead of negative.

[56] We note that our simple charging model does not predict large enough negative potentials for electron temperatures below 100 eV. We have considered several possible reasons for this. First of all, in the lunar wake, the electron temperature increases dramatically. However the ion temperature does not display such a dramatic increase [*Clack et al.*, 2004]. This would invalidate our assumption of electron and ion distributions with the same density and temperature in our model. Therefore we recalculate our model predictions for a constant ion temperature of 10 eV (but increasing electron temperature). As shown in Figure 12, this change does indeed increase the predicted magnitude of the negative potential. The work of [*Farrell et al.*, 2008] provides an additional possibility, suggesting that at the edge of the plasma front refilling the wake, electron density may exceed ion density (breaking quasi-neutrality over scale lengths much larger than a Debye length). We therefore calculate a new charging model with an ion density only half as large as the electron density. Again, this increases the predicted magnitude of the negative surface potential. We consider that either of these possibilities could help explain the large negative potentials encountered near the edges of the lunar wake. However, we note that if either of these phenomena actually occurs, they will also affect the spacecraft potential and our determination of electron parameters in a complicated fashion. The lunar wake represents a very complex environment, and a full description remains challenging. In addition to the factors already considered, ions also have a significant flow velocity along magnetic field lines into the wake [*Ogilvie et al.*, 1996; *Clack et al.*, 2004]. Furthermore, an ambipolar electric field exists across the wake boundary [*Halekas et al.*, 2005b], and some of the potential drop observed between the spacecraft and the surface could result from this ambipolar field (not associated with the surface). At this point, we can only say that lunar wake charging data appear to support a model of secondary emission with δ_M of 1.1–1.3, reasonably consistent with our results from the terrestrial magnetosphere.

8. Lunar Surface Potential During a Solar Energetic Particle Event

[57] As a final exercise, we consider the lunar surface potential during a large SEP event on 6 May 1998 previously investigated by *Halekas et al.* [2007]. For this event, with occasionally quite high fluxes of energetic charged particles, a determination of the LP spacecraft potential currently remains out of reach since we have not determined how to self-consistently fold in the effects of high energy particles not measured directly by LP. However, during most of this time period, electron temperatures remained such that secondary emission from the spacecraft should prevent significant negative spacecraft charging, so the correction for the spacecraft potential may not prove significant. We therefore use our same methodology for determining the lunar surface potential, but without any correction for the spacecraft potential. In addition, we utilize a combination of LP electron data and high energy electron data from SOHO [*Muller-Mellin et al.*, 1995], as described in *Halekas et al.* [2007], to determine the input electron spectrum. We fit the combined electron spectrum to a two-component distribution and show the resulting density and temperature components in Figure 13. The low energy components n_1 and T_1 behave very much like the density and temperature for a typical orbit in the solar wind and lunar wake, but with generally much higher electron temperatures than usually observed in the lunar wake. The high energy components of the fits, meanwhile, clearly show an injection of energetic electrons at ~08:00.

[58] The lunar surface potential in the lunar wake displays elevated values of close to −1 kV (several times larger than typical wake values) throughout this already disturbed time period. However, coinciding with the energetic electron injection, the lunar surface potential dramatically increases to peak values close to −4 kV, consistent with previous results from *Halekas et al.* [2007]. In Figure 14, we plot the magnitude of the negative nightside potential in the wake against the temperature of the low energy electron component. We show three representative fits, all assuming a constant ion temperature of 10 eV as in the preceding section. We note that energetic ions will in general affect

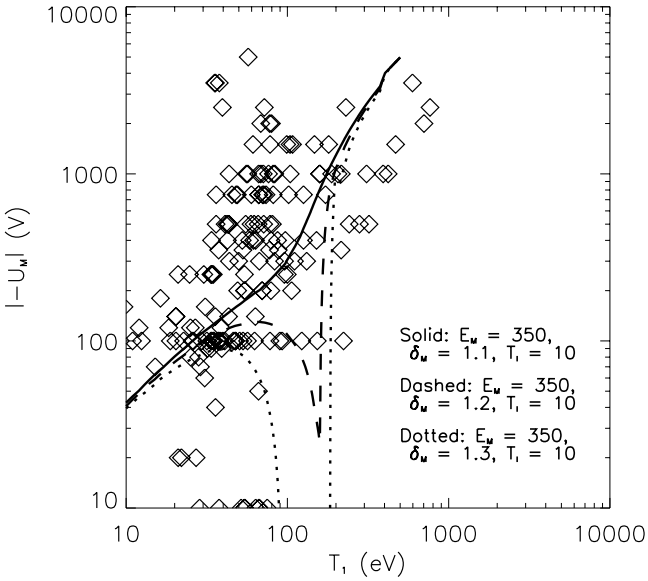

Figure 14. Magnitude of negative nightside lunar surface potentials observed in the lunar wake during the SEP event shown in Figure 13, as a function of downward-going electron temperature (low energy component only), with representative fits.

the charging balance; however, during this particular injection, energetic electron currents greatly exceeded energetic ion currents [*Halekas et al.*, 2007], allowing us to reasonably neglect energetic ions. The charging behavior during this SEP event shows reasonable agreement with the charging model we have constructed. In Figure 15, when we utilize both components of the distribution to construct a total electron temperature, we find even a slightly better agreement with our charging model, though significant scatter still exists (not surprising given the intrinsic uncertainty in many steps of this calculation—for instance, correcting self-consistently for the spacecraft potential during this SEP event would likely improve the fit since accounting for spacecraft charging at the highest electron temperatures would also increase the magnitudes of the estimated lunar surface potentials). We therefore find lunar surface charging during this SEP event consistent with roughly the same secondary emission parameters determined for orbits in the terrestrial magnetosphere and the quiet-time solar wind wake.

9. Conclusions

[59] We have presented the first results of a reanalysis of selected LP ER data. For the first time, we have successfully corrected for the effects of spacecraft charging and employed a self-consistent method to utilize the entire measured electron distribution to determine the lunar surface potential. We can now measure the lunar surface potential with respect to the ambient plasma (in sunlit or shadowed conditions) with high fidelity whenever the lunar surface floats to a negative potential larger than ~-20 V. In addition, thanks to knowledge of the LP spacecraft potential, we can now accurately determine the properties of the downward-going plasma electrons that largely control lunar surface charging. Any future mission wishing to investigate lunar surface charging should include (at a minimum), spacecraft potential measurements, and both ion and electron measurements. However, even lacking any measurements of spacecraft potential or ion fluxes, we have now demonstrated the ability to address the lunar surface charging problem in more detail than previously possible.

[60] By utilizing our new methodology for selected time periods, we have found typical nightside potentials in the terrestrial magnetotail lobes of ~-100 V and of several hundred volts to a kilovolt negative in the plasma sheet. On the dayside, meanwhile, we only observe significant negative charging in the terrestrial plasma sheet. In the lunar wake, we find negative potentials of ~-200 V near the boundary of the wake, with smaller negative potentials in the central wake. During SEP events, meanwhile, the lunar nightside potential can increase to values of ~-4 kV. We summarize all of the surface potential results in Table 1.

[61] The presence of negative charging in sunlight, even in the energetic plasma sheet, implies either much lower photoemission from lunar regolith in situ than suggested by laboratory measurements or nonmonotonic potentials above the lunar surface. Meanwhile, lunar surface charging in shadow suggests secondary emission from lunar regolith in situ with a somewhat lower yield than suggested from laboratory experiments.

[62] For the first time, we can make measurements of lunar surface charging from orbit with sufficient fidelity to determine how the lunar surface responds to incident solar photons and plasma currents. We can utilize this methodology not only to characterize the lunar near-surface electric field environment but also to determine material properties of the lunar regolith in situ.

[63] These new techniques open the door for future studies of the variation of lunar surface potentials as a function of temporal and spatial variations in input currents

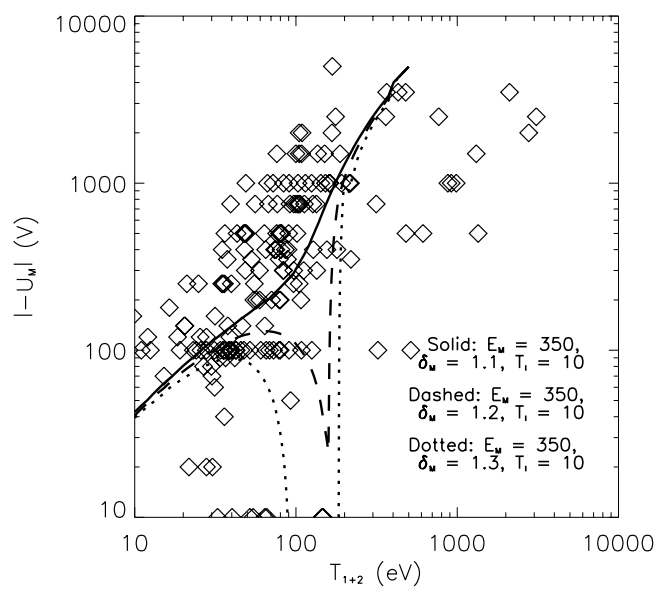

Figure 15. Same data as shown in Figure 14, but plotted as a function of total downward-going electron temperature (accounting for both high and low energy components).

and as a function of location and material characteristics of the surface. In addition, we now possess sufficiently accurate surface charging data to compare to the increasingly sophisticated theoretical predictions now available.

[64] **Acknowledgments.** This work was supported by NASA grants NNG06GJ23G and NNX07AG10G.

[65] Wolfgang Baumjohann thanks Joseph Wang and another reviewer for their assistance in evaluating this paper.

References

Anderson, K. A., R. P. Lin, R. E. McGuire, and J. E. McCoy (1975), Measurement of lunar and planetary magnetic fields by reflection of low energy electrons, *Space Sci. Instrum.*, *1*, 439–470.

Bedingfield, K. L., R. D. Leach, and M. B. Alexander (1996), Spacecraft system failures and anomalies attributed to the natural space environment, *NASA Reference Publication*, 1390.

Benson, J. (1977), Direct measurements of the plasma screening length and surface potential near the lunar terminator, *J. Geophys. Res.*, *82*, 13, 1917–1920.

Berg, O. E., H. Wolf, and J. W. Rhee (1976), Lunar soil movement registered by the Apollo 17 cosmic dust experiment, in *Interplanetary Dust and Zodiacal Light*, edited by H. Elsässer and H. Fechtig, pp. 233–237, Springer-Verlag, Berlin.

Clack, D., J. C. Kasper, A. J. Lazarus, J. T. Steinberg, and W. M. Farrell (2004), Wind observations of extreme ion temperature anisotropies in the lunar wake, *Geophys. Res. Lett.*, *31*, L06812, doi:10.1029/2003GL018298.

Cladis, J. B., W. E. Francis, and R. R. Vondrak (1994), Transport towards Earth of ions sputtered from the Moon's surface by the solar wind, *J. Geophys. Res.*, *99*(A1), 53–64.

Criswell, D. R. (1973), Horizon-glow and the motion of lunar dust, in *Photon and Particle Interactions with Surfaces in Space*, edited by R. J. L. Grard and D. Reidel, pp. 545–556, Dordrecht, Netherlands.

Davis, V. A., M. J. Mandell, and M. F. Thomsen (2003), Characterization of magnetospheric spacecraft charging environments using the LANL magnetospheric plasma analyzer data set, *NASA/CR-2003-212745*.

Doe, S. J., O. Burns, D. Pettit, J. Blacic, and P. W. Keaton (1994), The levitation of lunar dust via electrostatic forces, in *Engineering, Construction, and Operations in Space*, pp. 907–915, Am. Soc. Civ. Eng., New York.

Eriksson, A. I., L. Wedin, J.-E. Wahlund, and B. Holback (1998), Analysis of Freja charging events: Modelling of Freja observations by spacecraft charging codes, *ESTEC Report SPEE-WP120-TN*.

Escoubet, C. P., A. Pederson, R. Schmidt, and P. Lindqvist (1997), Density in the magnetosphere inferred from the ISEE-1 spacecraft potential, *J. Geophys. Res.*, *102*, 17,595–17,609.

Farrell, W. M., T. J. Stubbs, J. S. Halekas, G. T. Delory, M. R. Collier, R. R. Vondrak, and R. P. Lin (2008), Loss of solar wind plasma neutrality and affect on surface potentials near the lunar terminator and shadowed polar regions, *Geophys. Res. Lett.*, *35*, L05105, doi:10.1029/2007GL032653.

Fenner, M. A., J. W. Freeman, and H. K. Hills (1973), The electric potential of the lunar surface, *Proc. Lunar Planet Sci. Conf., 4th*, *3*, 2877–2887.

Feuerbacher, B., M. Anderegg, B. Fitton, L. D. Laude, R. F. Willis, and R. J. L. Grard (1972), Photoemission from lunar surface fines and the lunar photoelectron sheath, *Proc. Lunar Planet Sci. Conf.*, *3*, 2655–2663.

Freeman, J. W., and M. Ibrahim (1975), Lunar electric fields, surface potential and associated plasma sheaths, *Moon*, *14*, 103–114.

Freeman, J. W., Jr., M. A. Fenner, and H. K. Hills (1973), Electric potential of the Moon in the solar wind, *J. Geophys. Res.*, *78*, 4560–4567.

Freeman, J. W., Jr., M. A. Fenner, H. K. Hills, R. A. Lindeman, R. Medrano, and J. Meister (1972), Suprathermal ions near the moon, *Icarus*, *16*, 328–338.

Fu, J. H. M. (1971), Surface potential of a photoemitting plate, *J. Geophys. Res.*, *76*, 2506–2509.

Goldstein, B. E. (1974), Observations of electrons at the lunar surface, *J. Geophys. Res.*, *79*, 23–35.

Guernsey, R. L., and J. H. M. Fu (1970), Potential distribution surrounding a photo-emitting plate in a dilute plasma, *J. Geophys. Res.*, *75*(16), 3193–3199.

Halekas, J. S., D. L. Mitchell, R. P. Lin, L. L. Hood, and M. H. Acuña (2002), Evidence for negative charging of the lunar surface in shadow, *Geophys. Res. Lett.*, *29*(10), 1435, doi:10.1029/2001GL014428.

Halekas, J. S., et al. (2007), Extreme lunar surface charging during solar energetic particle events, *Geophys. Res. Lett.*, *34*, L02111, doi:10.1029/2006GL028517.

Halekas, J. S., R. P. Lin, and D. L. Mitchell (2003), Inferring the scale height of the lunar nightside double layer, *Geophys. Res. Lett.*, *30*(21), 2117, doi:10.1029/2003GL018421.

Halekas, J. S., R. P. Lin, and D. L. Mitchell (2005a), Large negative lunar surface potentials in sunlight and shadow, *Geophys. Res. Lett.*, *32*, L09102, doi:10.1029/2005GL022627.

Halekas, J. S., S. D. Bale, D. L. Mitchell, and R. P. Lin (2005b), Magnetic fields and electrons in the lunar plasma wake, *J. Geophys. Res.*, *110*, A07222, doi:10.1029/2004JA010991.

Hilchenbach, M., D. Hovestadt, B. Klecker, and E. Mobius (1991), Detection of singly ionized energetic lunar pick-up ions upstream of Earth's bow shock, in *Solar Wind Seven*, edited by E. Marsch and G. Schwenn, pp. 150–155, Pergamon, New York.

Hilchenbach, M., D. Hovestadt, B. Klecker, and E. Mobius (1993), Observation of energetic lunar pick-up ions near Earth, *Adv. Space Res.*, *13*(10), 321–324.

Hills, H. K., J. Meister, C. Richard, R. Vondrak, and J. W. Freeman Jr. (1972), Suprathermal Ion Detector Experiment (Lunar Ionosphere Detector), in *Apollo 15 Preliminary Science Report*, *NASA SP-289*.

Horányi, M. (1996), Charged dust dynamics in the solar system, *Annu. Rev. Astron. Astrophys.*, *34*, 383–418.

Horányi, M., B. Walch, S. Robertson, and D. Alexander (1998), Electrostatic charging properties of Apollo 17 lunar dust, *J. Geophys. Res.*, *103*, 8575–8580.

Knott, K. (1973), Electrostatic charging of the lunar surface and possible consequences, *J. Geophys. Res.*, *78*, 3172–3175.

Koons, H. C., J. E. Mazur, R. S. Selesnick, J. B. Blake, J. F. Fennell, J. L. Roeder, and P. C. Anderson (2000), The impact of the space environment on space systems, *6th Spacecraft Charging Technology Conference*, AFRL-VS-TR-20001578.

Leach, R. D. (1995), Spacecraft system failures and anomalies attributed to the natural space environment, *AIAA 1995 Space Programs and Technologies Conference*.

Lindeman, R., J. W. Freeman, and R. R. Vondrak (1973), Ions from the lunar atmosphere, *Proc. Lunar Planet Sci. Conf. 4th.*, 2889–2896.

Mall, U., E. Kirsch, K. Cierpka, B. Wilken, A. Söding, F. Neubauer, G. Gloeckler, and A. Galvin (1998), Direct observation of lunar pick-up ions near the Moon, *Geophys. Res. Lett.*, *25*(20), 3799–3802.

Manka, R. H. (1973), Plasma and potential at the lunar surface, in *Photon and Particle Interactions with Surfaces in Space*, edited by R. J. L. Grard and D. Reidel, pp. 347–361, Dordrecht, Netherlands.

McCoy, J. E. (1976), Photometric studies of light scattering above the lunar terminator from Apollo solar corona photography, *Proc. Lunar Planet Sci. Conf.*, *7*, 1087–1112.

McCoy, J. E., and D. R. Criswell (1974), Evidence for a high altitude distribution of lunar dust, *Proc. Lunar Planet Sci. Conf.*, *5*, 2991–3005.

Muller-Mellin, R., H. Kunow, and V. Fleissner, et al. (1995), COSTEP—Comprehensive Suprathermal and Energetic Particle Analyser, *Sol. Phys.*, *162*, 483–504.

Nitter, T., and O. Havnes (1992), Dynamics of dust in a plasma sheath and injection of dust into the plasma sheath above moon and asteroidal surfaces, *Earth Moon Planets*, *56*, 7–34.

Nitter, T., O. Havnes, and F. Melandsø (1998), Levitation and dynamics of charged dust in the photoelectron sheath above surfaces in space, *J. Geophys. Res.*, *103*, 6605–6620.

O'Brien, J. Brian, and D. L. Reasoner (1971), Charged-particle lunar environment experiment, in *Apollo 14 Preliminary Science Report, NASA SP-272*.

Ogilvie, K. W., J. T. Steinberg, R. J. Fitzenreiter, C. J. Owen, A. J. Lazarus, W. M. Farrell, and R. B. Torbert (1996), Observations of the lunar plasma wake from the WIND spacecraft on December 27, 1994, *Geophys. Res. Lett.*, *10*, 1255–1258.

Pederson, A. (1995), Solar wind and magnetosphere plasma diagnostics by spacecraft electrostatic potential measurements, *Ann. Geophys.*, *13*, 118–129.

Reasoner, D. L., and W. J. Burke (1972), Characteristics of the lunar photoelectron layer in the geomagnetic tail, *J. Geophys. Res.*, *77*, 6671–6687.

Rennilson, J. J., and D. R. Criswell (1974), Surveyor observations of lunar horizon-glow, *Moon*, *10*, 121–142.

Rhee, J. W., O. E. Berg, and H. Wolf (1977), Electrostatic dust transport and Apollo 17 LEAM experiment, in *COSPAR Space Research XVII*, pp. 627–629, Pergamon, New York.

Rich, F. J., D. L. Reasoner, and W. J. Burke (1973), Plasma sheet at lunar distance: Characteristics and interactions with the lunar surface, *J. Geophys. Res.*, *78*(34), 8097–8112.

Samir, U., K. H. Wright Jr., and N. H. Stone (1983), The expansion of a plasma into a vacuum: Basic phenomena and processes and applications to space plasma physics, *Rev. Geophys.*, *21*, 1631–1646.

Scudder, J. D., E. S. Sittler Jr., and H. S. Bridge (1981), A survey of the plasma electron environment of Jupiter: Voyager 1, *J. Geophys. Res.*, *86*, 8157–8179.

Scudder, J. D., X. Cao, and F. S. Mozer (2000), Photoemission current–spacecraft voltage relation: Key to routine, quantitative low-energy plasma measurements, *J. Geophys. Res.*, *105*(A9), 21,281–21,294.

Sickafoose, A. A., J. E. Colwell, M. Horányi, and S. Robertson (2002), Experimental levitation of dust grains in a plasma sheath, *J. Geophys. Res.*, *107*(A11), 1408, doi:10.1029/2002JA009347.

Singer, S. F., and E. H. Walker (1962), Photelectric screening of bodies in interplanetary space, *Icarus*, *1*, 7–12.

Stern, S. A. (1999), The lunar atmosphere: History, status, current problems, and context, *Rev. Geophys.*, *37*(4), 453–491.

Sternglass, E. J. (1954), The theory of secondary emission, Sci. Pap., 1772, Westinghouse Res. Lab., Pittsburgh, Pa.

Stubbs, T. J., R. R. Vondrak, and W. M. Farrell (2006), A dynamic fountain model for lunar dust, *Adv. Space Res.*, *37*(1), 59–66.

Stubbs, T. J., R. R. Vondrak, and W. M. Farrell (2007a), Impact of dust on lunar exploration, in *Dust in Planetary Systems* (Workshop, September 26–30 2005, Kauai, HI), edited by H. Krüger and A. L. Graps, pp. 239–244, ESA Publications, SP-643.

Stubbs, T. J., J. S. Halekas, W. M. Farrell, and R. R. Vondrak (2007b), Lunar surface charging: A global perspective using Lunar Prospector data, in *Dust in Planetary Systems* (Workshop, September 26–30 2005, Kauai, HI), edited by H. Krüger and A. L. Graps, pp. 181–184, ESA Publications, SP-643.

Stubbs, T. J., R. R. Vondrak, and W. M. Farrell (2007c), A dynamic fountain model for dust in the lunar exosphere, in *Dust in Planetary Systems* (Workshop, September 26–30 2005, Kauai, HI), edited by H. Krüger and A. L. Graps, pp. 185–190, ESA Publications, SP-643.

Whipple, E. C. (1981), Potentials of surfaces in space, *Rep. Prog. Phys.*, *44*, 1197–1250.

Willis, R. F., M. Anderegg, B. Feuerbacher, and B. Fitton (1973), Photoemission and secondary electron emission from lunar surface material, in *Photon and Particle Interactions with Surfaces in Space*, edited by R. J. L. Grard and D. Reidel, pp. 389–401, Dordrecht, Netherlands.

Zook, H. A., A. E. Potter, and B. L. Cooper (1995), The lunar dust exosphere and Clementine lunar horizon glow, *Proc. Lunar Planet Sci. Conf.*, *26*, 1577–1578.

Zook, H. A., and J. E. McCoy (1991), Large scale lunar horizon glow and a high altitude lunar dust exosphere, *Geophys. Res. Lett.*, *18*, 2117–2120.

G. T. Delory, J. S. Halekas, and R. P. Lin, Space Sciences Laboratory, University of California, Berkeley, CA 94720, USA. (jazzman@ssl.berkeley.edu)

W. M. Farrell, NASA Goddard Spaceflight Center, Greenbelt, MD 20771, USA.

T. J. Stubbs, Goddard Earth Sciences and Technology Center, University of Maryland Baltimore County, Baltimore, MD 21250, USA.